Influence of laser beam welding parameters on the microstructure and mechanical behavior of Inconel X750 superalloy

Abhishek Pariyar [a,b,c,*], Aashish John [c], Chandra S. Perugu [d], Vimal Edachery [c,e], Satish V. Kailas [c]

[a] Laboratory of Excellence on Design of Alloy Metals for Low-Mass Structure (Labex-DAMAS), Université de Lorraine, 57070 Metz, France
[b] Laboratoire d'Etude des Microstructures et de Mécanique des Matériaux (LEM3), Université de Lorraine, 57070 Metz, France
[c] Department of Mechanical Engineering, Indian Institute of Science, Bangalore 560012, India
[d] Department of Materials Engineering, Indian Institute of Science, Bangalore 560012, India
[e] Department of Mechanical Engineering, Indian Institute of Technology Madras, Chennai 600036, India

ARTICLE INFO

ABSTRACT

In welding, the process parameters influence the mechanical properties of the joint. However, such investigations on laser welding of Inconel X750 are lacking despite its industrial significance. We performed such an investigation in which three parameter combinations, out of seven, exhibited full laser penetration (S1 (75 mm/min, 800 W), S2 (75 mm/min, 1200 W), and S3 (150 mm/min and 1200 W)). Microstructural analysis exhibited changes in the grain and dendrite morphology with columnar to equiaxed transition from the fusion boundary to the interior. S3 exhibited superior mechanical properties than others due to the smaller grain size and fusion zone.

1. Introduction

Since the introduction of laser technology in the 1960s at Hughes Research Laboratories, the application of lasers in the field of material processing has rapidly increased [1]. Further, with the introduction of the laser as a joining tool, laser beam welding (LBW) has been used in various applications [2]. With the advantage of a high depth to width ratio, along with the reduced processing time, narrow fusion zone and heat affected zone (HAZ), little distortion of the workpiece, and high welding speed make LBW an ideal candidate for a wide range of applications including aerospace, military, power and automotive industries [3–7].

Ni-based superalloys and their composites are high-performance materials primarily used in the aerospace and nuclear power industries [4,8–12]. Inconel X750, in particular, is used for such applications due to its high -strength, ductility, fatigue, creep, oxidation, and corrosion resistance [8,13–15]. Such properties are due to the $\gamma'[Ni_3(Ti, Al)]$ phase along with primary MC-type carbides and secondary $M_{23}C_6$ carbide precipitates [13].

One of the most important aspects of welding is to study the effect that the process parameters have on the microstructure and mechanical properties of the welded joint. In this regard, several studies have been made on various grades of Inconel; however, such studies have been sparingly made on Inconel X750. Odabasi et al.[16], while performing LBW on Inconel 718, observed that the heat input and welding speed have a significant impact on the welding geometry. Egbewande et al. [17] observed a decrease in HAZ cracking with an increase in welding speed, during LBW of Inconel 738. This was because of the process instability leading to severe cracking during lower welding speeds. Jelorkhani et al. [18] observed an increase in weld strength and microhardness with the increase in laser power. Vemanaboina et al. [19] investigated the LBW of Inconel 625 and observed the narrow HAZ with a small amount of porosity. Even with the porosity, a comparable tensile strength was observed for the welded material, compared to the parent material. Caizzao et al. [4] conducted laser welding on Inconel 625 without filler metal or heat treatments and observed a decrease in grain size with a decrease in heat input which resulted in an improved mechanical property. An increase in porosity was also observed with the increase in heat input.

Although Inconel X750 has various applications, especially in the nuclear energy industry [20,21], the joining of this superalloy has not been performed using LBW. Hence, this part is still unexplored and through this work, we have attempted to study the laser welding behavior of this superalloy for the first time. We have optimized the process parameters for full laser penetration and

* Corresponding author at: Laboratory of Excellence on Design of Alloy Metals for Low-Mass Structure (Labex-DAMAS), Université de Lorraine, 57070 Metz, France.
E-mail address: azp560012@gmail.com (A. Pariyar).

Table 1
The different values of the traverse speed and power used for laser welding of Inconel X750.

Sl No	Traverse Speed (mm/min)	Power (W)
1	75	1200
2	150	1200
3	300	1200
4	300	800
5	150	800
6	75	800
7	75	400

Table 2
The process parameter combinations that exhibited full laser penetration.

Sample Name	Traverse Speed (mm/min)	Power (W)
S1	75	800
S2	75	1200
S3	150	1200

thoroughly investigated its effect on the microstructure and mechanical properties of the material. The results of this study would be helpful for industrial applications and for other researchers wanting to explore further in this area. Furthermore, such studies will also have an impact on the laser-based additive manufacturing of Inconel X750.

2. Materials and methods

Inconel X750 sheet in hot rolled condition (chemical composition in [13]) of 1.2 mm thickness was used. Bead-on-plate (BOP) welding was performed using a continuous Nd: YAG laser with a spot diameter of 0.6 mm under argon (80 %) + CO_2 (20 %) gas at a 30 l/min flow rate. To find the parameters that allowed complete penetration depth, experiments were performed with varying traverse speeds and laser powers. The combinations of these two parameters are shown in Table 1. Out of those, three processing
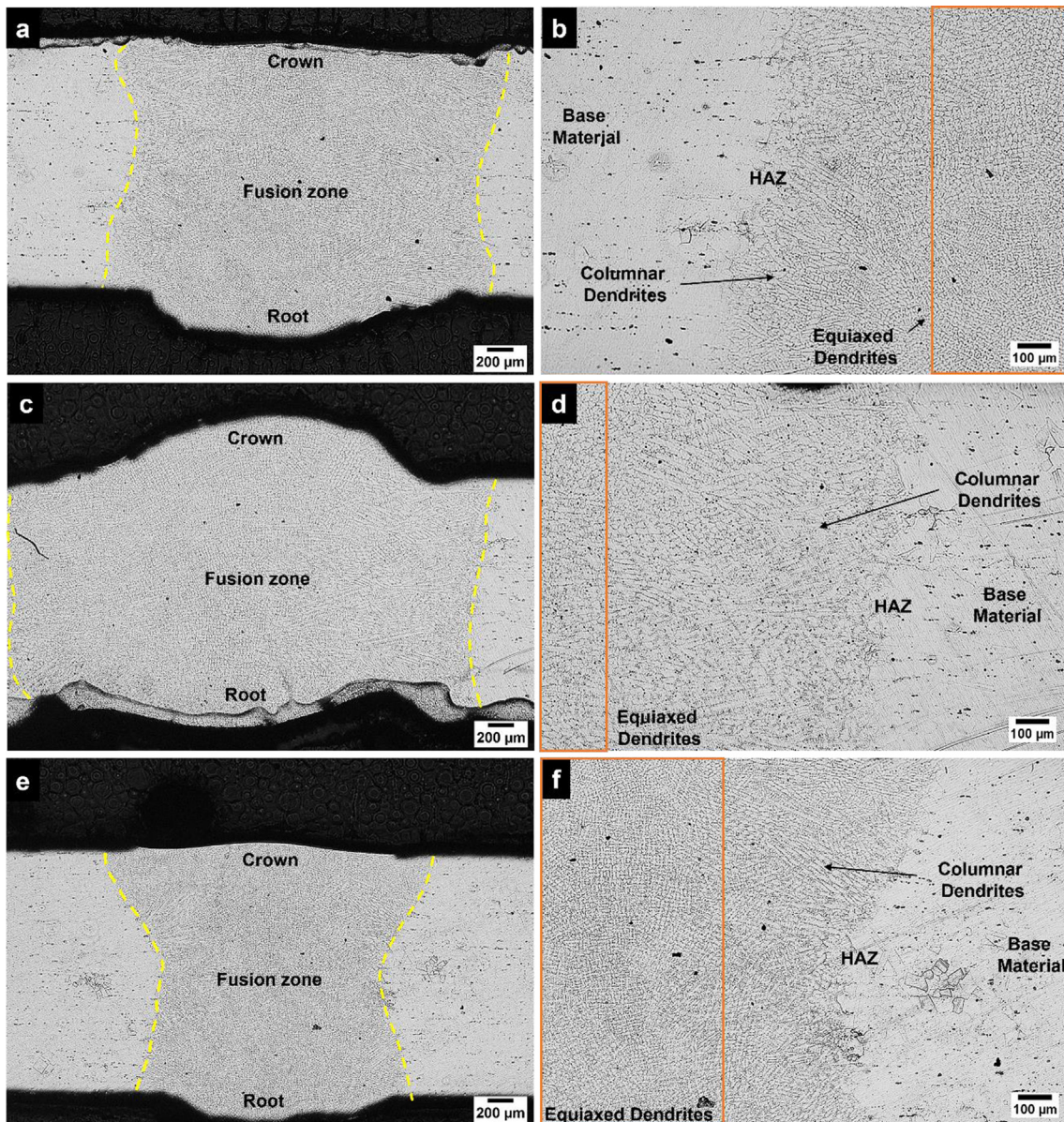

Fig. 1. (a) Optical micrograph (OM) of the weld cross-section of S1 showing the full depth of laser penetration. (b) OM of the fusion zone boundary of S1 showing the columnar and equiaxed dendrites. (c) Weld cross-section of S2 showing full laser penetration. (d) Fusion zone boundary of S2. (e) Weld cross-section of S3 showing full laser penetration. (f) Fusion zone boundary of S3.

conditions exhibited complete laser penetration which is shown in Table 2. Microstructural characterization and mechanical testing were performed only for these three weld conditions. For this, the specimens were cut using wire electro-discharge machining. The microstructures of the samples were analyzed at the fusion zone and the heat-affected zone (HAZ) using an optical microscope (Carl Zeiss MAT 200) and electron backscattered diffraction (EBSD) (FEI Nova NanoSEM 450). Tensile tests were performed as per the ASTM-E8 standard on a UTM machine (INSTRON − 5967) at a strain rate of 10^{-3} s^{-1}. The 6 mm gauge length tensile specimens were cut perpendicular to the laser traverse direction.

3. Results and discussion

In Fig. 1, the optical micrographs of the welded specimens are shown. Fig. 1a shows the cross-section of S1 and the full thickness of the specimen. As we move from the top (crown) to the bottom (root), it can be observed that the laser penetrated the specimen fully throughout the thickness. The fusion zone has been demarcated by yellow dashed lines. The fusion zone can be distinguished from the base material due to the dendritic structure that spans from the crown to the root. The average width of the fusion zone was ∼ 2.5 mm. Fig. 1b shows the fusion zone, heat affected zone (HAZ) and the unaffected base material region at a higher magnification. It can be observed in this figure that the fusion zone was indeed comprised of dendrites. The difference in the dendritic

structure near the fusion boundary and the interior of the fusion zone can be observed. The dendrites were columnar in morphology in the former and equiaxed in the latter.

In Fig. 1c, the full cross-section of S2 is shown. A similar dendritic structure in the fusion zone could be observed for this specimen as well. However, the average width of the fusion zone was larger in S2 (∼3.2 mm) compared to S1. Moreover, the fusion zone shape was also distorted when compared to the other specimens. In Fig. 1d, similar to Fig. 1b, columnar dendrites near the fusion boundary and equiaxed dendrites in the fusion zone interior were observed. However, the fusion zone area covered by the columnar dendrites was larger compared to S1.

In Fig. 1e, the complete weld cross-section of S3 is shown. The fusion zone exhibited an 'X' shape which is associated with strong Marangoni convection due to the strong surface tension gradient of the liquid metal on both sides of the weld [22]. The average fusion zone width for S3 was the smallest (∼1.8 mm) compared to the other two specimens. This suggests that specimen S3 experienced the detrimental effects of welding the least. In contrast, it was the opposite for specimen S2. Like the other two welded specimens, dendritic structure in the fusion zone could be observed in this specimen as well with similar distribution of the columnar and equiaxed dendrites (Fig. 1f).

In all three welded specimens, there was a columnar to equiaxed transition in the dendrite morphology from the fusion boundary to the interior of the fusion zone. The dendrite morphology is dependent on the temperature gradient G, solidification rate R
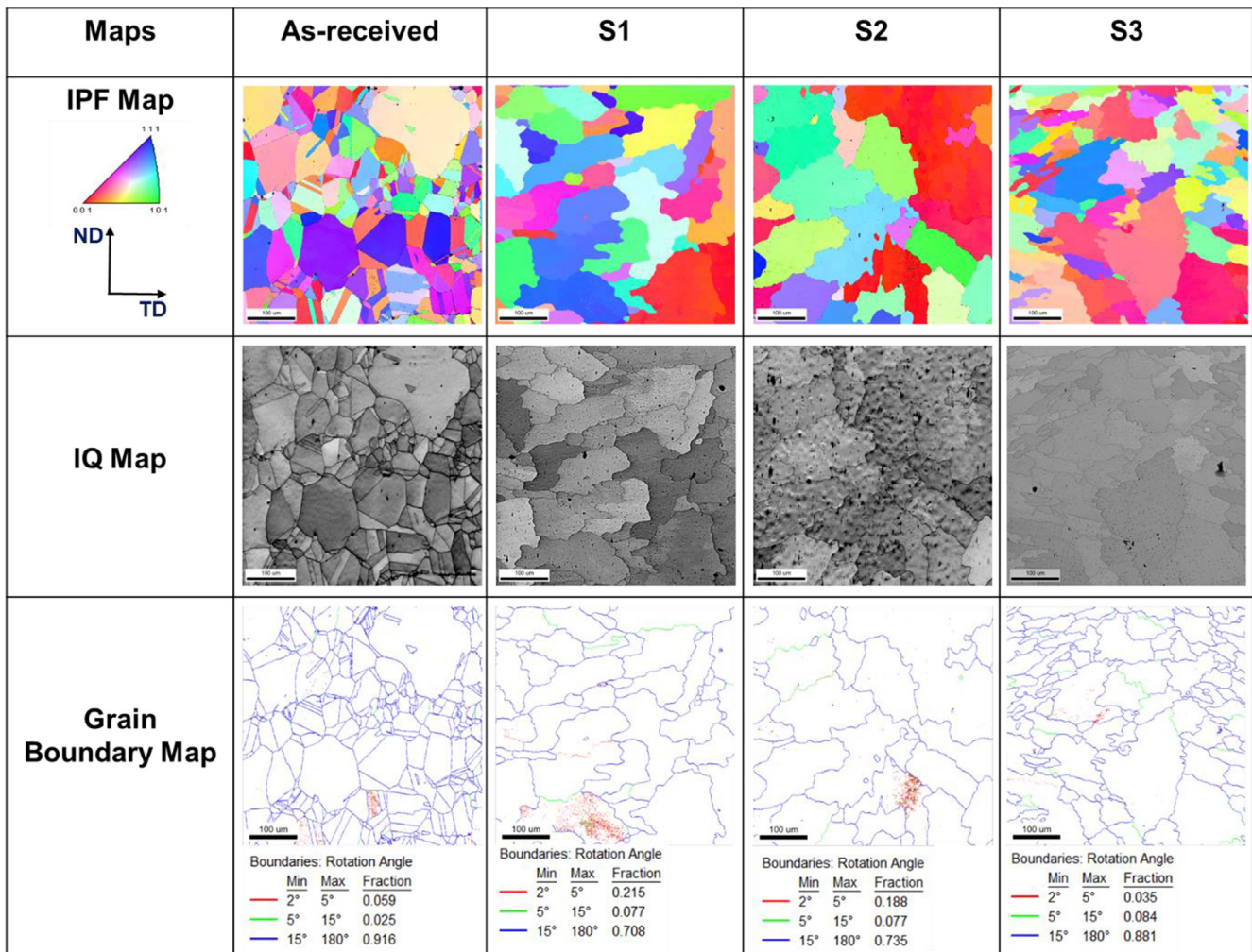

Fig. 2. IPF, IQ, and grain boundary maps of the base material (as-received) and the fusion zone centers of S1, S2, and S3 specimens.

and constitutional supercooling degree. It has been reported that the *G/R* ratio decreases from the boundary to the interior while it is vice versa for the constitutional supercooling degree. A higher value of the *G/R* ratio results in columnar dendrites, whereas lower values produce equiaxed dendrites [23]. Previous studies on the LBW of Inconel 617 [22], 718 [24] and 738 [17] have also reported the formation of dendrites in the fusion zone of the welds. It has also been observed in these studies that the precipitate distribution of the superalloy changes after LBW. The interdendritic regions have been reported to be rich in MC carbides, γ-γ' eutectic and nano-sized γ' precipitates [25]. Hence, in the fusion zone, microsegregation of the solute atoms could be expected.

Amongst the three welding conditions, S2 exhibited the largest fusion zone and S3 the smallest. It is known that the size of the fusion zone is directly affected by the processing parameters. A larger size is indicative of high-heat conditions as the volume of the melted metal is more in such scenarios [22]. Hence, Specimen S2 experienced higher heat conditions compared to S1 and S3.

In Fig. 2, the inverse pole figure (IPF), image quality (*IQ*), and grain boundary maps of the base material (as-received) and the welded specimens (center of the fusion zone) are shown. The base material possessed equiaxed grains with an average size (area fraction) of ~ 69 μm. Additionally, twins could also be observed in this specimen. In the grain boundary map, the red color indicated sub-grain boundaries (misorientation angle 2° to 5°), green color indicated low angle boundaries (LAB, misorientation angle 5° to 15°) and the blue color indicated high angle grain boundaries (HAGB, misorientation angle > 15°). The specimen comprised a high fraction (91.6 %) of HAGB.

In the EBSD maps of the welded specimens, there was a change in the grain morphology compared to the base material. The grains were nearly-equiaxed in shape but had irregular looking boundaries. Additionally, twin boundaries were not present as well. The average grain size in S1 (area fraction) was ~ 110 μm. Hence, there was an increase in the grain size compared to the base material. For S2, the grain morphology was similar to S1; however, the aver-
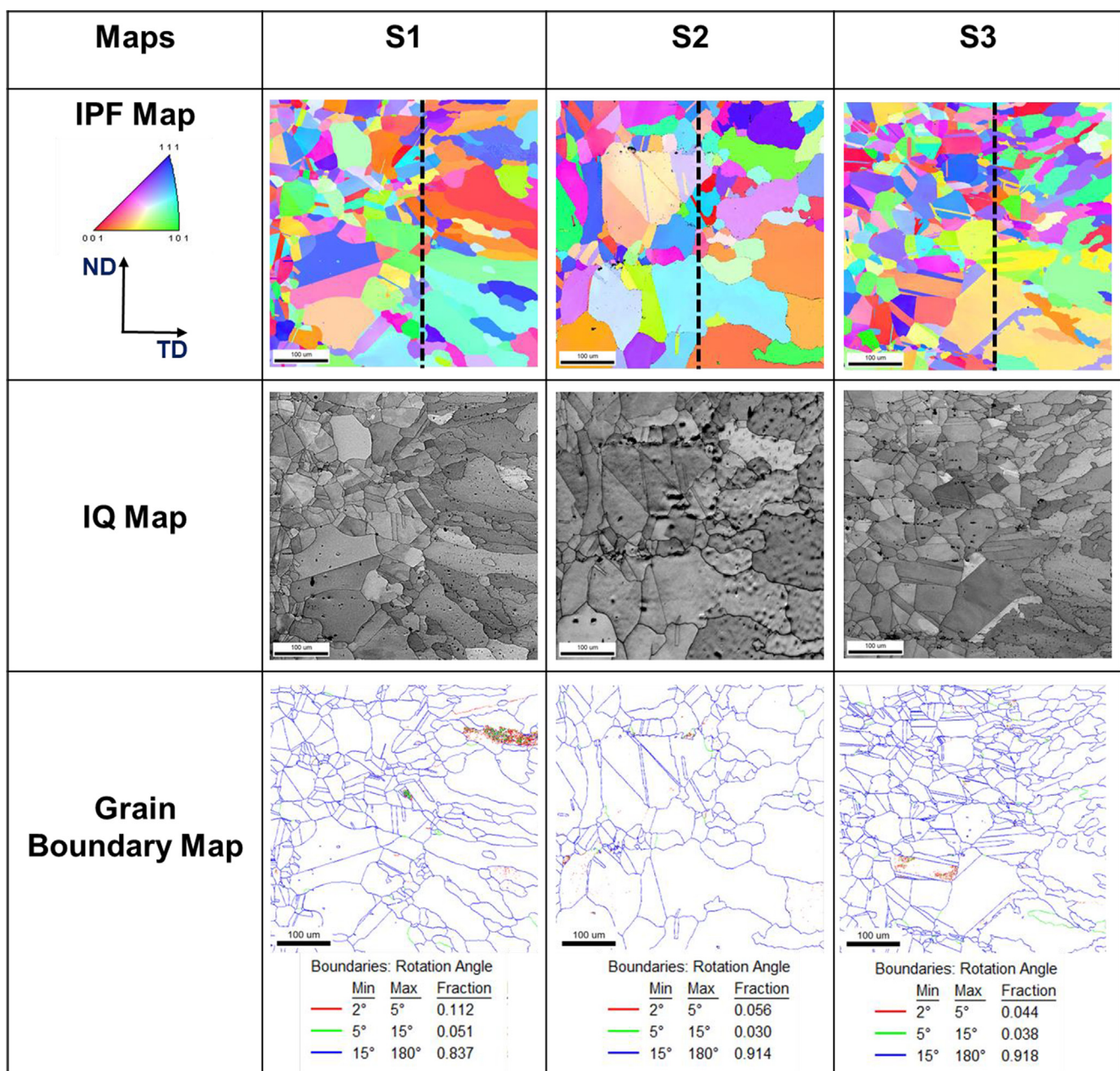

Fig. 3. IPF, *IQ*, and grain boundary maps showing the fusion zone boundary in S1, S2, and S3 specimens.

age grain size was ∼ 150 μm. The grain size is dependent on the cooling rate ($G \times R$) of the fusion zone. It has been reported that with the increase in the laser power, the cooling rate decreases. This is because more energy is absorbed thus increasing the melt pool size and decreasing the temperature gradient and solidification rate. Hence, the cooling rate decreases with the increase in laser power. This in turn leads to coarsening of the grains [26]. Hence, the increase in the grain size in S2 compared to S1 can be attributed to the lower cooling rates as the power was increased from 800 W to 1200 W, while the traverse speed was kept constant. In other words, the heat input was higher in S2 [27,28].

For specimen S3, it can be observed that the grain size was smaller compared to S1 and S2. The average grain size in S3 was ∼ 90 μm which is a 40 % reduction compared to S2. As mentioned earlier, the grain size is dependent on the cooling rate. However, apart from the laser power, the cooling rate is also dependent on the laser traverse speed. The cooling rate increases with the increase in the traverse speed which eventually leads to a decrease in the grain size [29]. In the case of S3, the traverse speed was increased compared to S2, while keeping the laser power constant. This increase in the traverse speed increased the cooling rate which in turn decreased the grain size almost by 40 %.

In the grain boundary maps, it could be observed that all the welded specimens exhibited a higher fraction of LABs compared to the base material. This would possibly have a consequence in strengthening the material [30].

In Fig. 3, the EBSD maps of the fusion zone-base material boundary containing the HAZ are shown for the welded specimens. The black dashed line demarcates the boundary between the fusion zone and the base material. On the left side of the dashed line is the base material and, on the right, is the fusion zone. It has been reported that the fusion zone boundary generally exhibits columnar grains due to epitaxial growth occurring from the base material grains during LBW [31]. As mentioned earlier, the change in the grain morphology from the fusion zone boundary to the interior is dependent on the *G/R* ratio with a high value resulting in epitaxial growth at the boundaries and a low value, in equiaxed grains [32]. The columnar grains at the fusion boundary can be observed in the *IQ* maps. In all the maps for the welded specimens, twin boundaries disappeared as we move from the left to the right.

Another important thing to note in all three specimens in both the optical micrographs and the EBSD maps was the absence of solidification cracks. Such cracks are normally observed in the fusion zone or HAZ during LBW [17]. In this regard, one of the key parameters that control such a phenomenon is the welding speed (traverse speed) as it directly influences the amount of stress generated. Generally, higher welding speeds induce higher thermal gradients and thermal stress in HAZ. Moreover, Shinozaki et al. [33] have shown that solidification cracking is also dependent on the grain size of the fusion zone, with smaller grain sizes (∼69 μm) being less susceptible to such cracks in LBW than the larger ones (∼210 μm). Such an effect could be prevalent in the present work as well.

In Fig. 4, the engineering stress–strain curves for the base material and the welded specimens are shown. The 0.2 % yield and the ultimate tensile strength (UTS) for the base material were 444 MPa and 909 MPa, respectively. The percentage elongation value was 76 %. The 0.2 % yield strengths (YS) for specimens S1, S2, and S3 were 492 MPa, 427 MPa, and 504 MPa, respectively. The UTS values were 859 MPa, 779 MPa, and 901 MPa, respectively. Their percentage elongation values were 43 %, 39 %, and 53 %, respectively. It can be observed from the tensile curves that amongst the welded specimens, S3 possessed the most superior mechanical properties and S2, the worst. In the optical micrographs, it was observed that the fusion zone width for S3 was the smallest and vice-versa for S2. This also indicated that more energy was absorbed in S2 compared
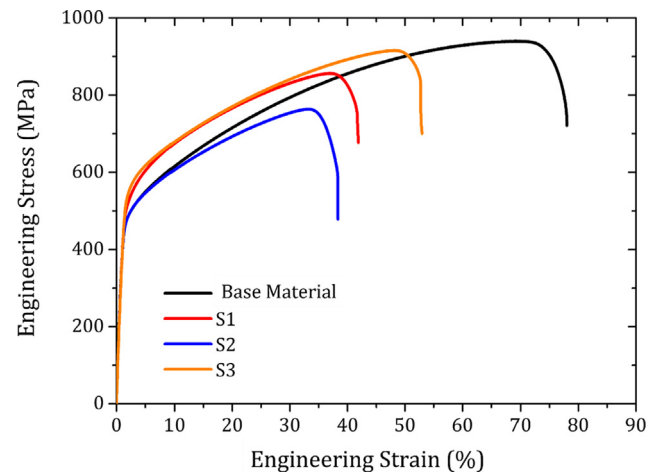

Fig. 4. Engineering stress–strain curves for the base material, S1, S2, and S3 specimens.

to S1 and S3. Hence, the detrimental effects of large energy input were evident in the tensile curve of S2. Thus, under these conditions, it is appropriate to use the parameter combination of S3 for laser welding while that of S2 should be avoided.

In the EBSD maps, it was observed that there was a difference in the grain size of the welded specimens. S3 possessed the smallest grain size and S2, had the largest. One of the strengthening mechanisms that are active in such welded specimens is the grain and substructure strengthening also called the Hall-Petch effect expressed as [34,35]:

$$\sigma_g = \sigma_o + kd^{-1/2} \tag{1}$$

where σ_0 is the internal back stress or the frictional stress to the motion of dislocation glide, d is the grain size and k is the Hall-Petch slope. By taking the ratios of the grain sizes it can be calculated that the yield strength of S3 was 1.3 times that of S2. Whereas the ratio of their experimentally measured yield strengths was 1.2. Hence, this suggests that the difference in the yield strengths of the welded specimens was proportional to the difference in their grain sizes. In the grain boundary maps (Fig. 2), the welded specimens also exhibited a higher fraction of the LABs. Such substructures also tend to strengthen the material when present and has been observed to be active in laser-welded specimens of other Ni-based superalloys [30].

4. Conclusions

In this work, the effects of the laser welding processing parameters on the microstructure and the mechanical behavior of Inconel X750 were studied. The following conclusions can be drawn from the results obtained:

1. Full laser penetration was observed only in three parameter combinations, namely, S1 (75 mm/min, 800 W), S2 (75 mm/min, 1200 W), and S3 (150 mm/min, 1200 W).
2. All the welded specimens exhibited dendritic structure in their fusion zone with columnar dendrites near the fusion zone boundary and equiaxed dendrites in the fusion zone interior. The average width of the fusion zone was the largest for specimen S2 and the least for specimen S3. Hence, the detrimental effects of heat input were the most for the former and the least for the latter.
3. The EBSD data of the fusion zones revealed the presence of grains nearly equiaxed in shape in the fusion zone interior and columnar near the fusion zone boundary. Specimen S2

exhibited the largest grain size (∼150 μm), whereas S3, had the smallest (∼90 μm). Hence, there was a 40 % reduction in the grain size.

4. Amongst the welded specimens, S3 exhibited the most superior mechanical properties which could be attributed to grain and substructure strengthening whereas S2 had the worst. The difference in the strength could be attributed to the difference in the grain sizes between the specimens. Hence, for the LBW of this superalloy, the parameter combination of S3 was the most appropriate.

Declaration of Competing Interest

The authors declare that they have no known competing financial interests or personal relationships that could have appeared to influence the work reported in this paper.

Acknowledgments

References

[1] Maiman TH. Stimulated optical radiation in ruby; 1960.
[2] Houldcroft PT. Welding process technology. Cambridge University Press; 1977.
[3] Katayama S. Handbook of laser welding technologies. Elsevier; 2013.
[4] Caiazzo F, Alfieri V, Cardaropoli F, Sergi V. Investigation on edge joints of Inconel 625 sheets processed with laser welding. Opt Laser Technol 2017;93:180–6.
[5] Choudhury B, Chandrasekaran M. Investigation on welding characteristics of aerospace materials–A review. Mater Today: Proc 2017;4:7519–26.
[6] Hong JK, Park JH, Park NK, Eom IS, Kim MB, Kang CY. Microstructures and mechanical properties of Inconel 718 welds by CO2 laser welding. J Mater Process Technol 2008;201:515–20. https://doi.org/10.1016/j.jmatprotec.2007.11.224.
[7] Gobbi S, Zhang L, Norris J, Richter KH, Loreau JH. High powder CO2 and Nd-YAG laser welding of wrought Inconel 718. J Mater Process Technol 1996;56:333–45.
[8] Reed RC. The Superalloys: Fundamentals and Applications. Cambridge Core 2006. https://doi.org/10.1017/CBO9780511541285.
[9] Sonar T, Balasubramanian V, Venkateswaran T, Sivakumar D, Konovalov S. Effect of Delta Straight and Delta Pulsed Arc Modes on Weld Bead Geometry, Microstructure and Tensile Properties of InterPulsed GTCA-welded Inconel 718 Alloy Joints for Aerospace and Nuclear Applications. Trans Indian Inst Met 2022;75:503–12.
[10] De Bartolomeis A, Newman ST, Shokrani A. High-speed milling Inconel 718 using Electrostatic Minimum Quantity Lubrication (EMQL). Procedia CIRP 2021;101:354–7.
[11] de Souza RR, de Paiva RL, Gelamo RV, Machado AR, da Silva RB. Study on grinding of inconel 625 and 718 alloys with cutting fluid enriched with multilayer graphene platelets. Wear 2021;476:203697.
[12] Bakkar A, Ahmed MM, Alsaleh NA, Seleman M-M-E-S, Ataya S. Microstructure, wear, and corrosion characterization of high TiC content Inconel 625 matrix composites. J Mater Res Technol 2019;8:1102–10.
[13] Pariyar A, Edachery V, John A, Kailas SV. A comparative tribological study of Inconel X750 under surface hardened and non-hardened conditions. Surf Topogr: Metrol Prop 2021;9:. https://doi.org/10.1088/2051-672X/ac1bfb035020.
[14] Ramkumar KD, Ramanand R, Ameer A, Simon KA, Arivazhagan N. Effect of post weld heat treatment on the microstructure and tensile properties of activated flux TIG welds of Inconel X750. Mater Sci Eng A 2016;658:326–38. https://doi.org/10.1016/j.msea.2016.02.022.
[15] Peasura P, Poopat B. Investigation into the influence of post-weld heat treatment on the microstructure and hardness of Inconel X-750. Advances in Mechanical Engineering 2015;7:1687814015578396.
[16] Odabaşı A, Ünlü N, Göller G, Eruslu MN. A study on laser beam welding (LBW) technique: effect of heat input on the microstructural evolution of superalloy Inconel 718. Metall Mater Trans A 2010;41:2357–65.
[17] Egbewande AT, Buckson RA, Ojo OA. Analysis of laser beam weldability of Inconel 738 superalloy. Mater Charact 2010;61:569–74. https://doi.org/10.1016/j.matchar.2010.02.016.
[18] Jelokhani-Niaraki MR, B Mostafa Arab N, Naffakh-Moosavy H, Ghoreishi M. The systematic parameter optimization in the Nd: YAG laser beam welding of Inconel 625. The International Journal of Advanced Manufacturing Technology 2016;84:2537–46.
[19] Vemanaboina H, Gundabattini E, Akella S, Rao AUM, Buddu RK, Ferro P, et al. Mechanical and Metallurgical Properties of CO2 Laser Beam INCONEL 625 Welded Joints. Appl Sci 2021;11:7002.
[20] Zhang HK, Yao Z, Judge C, Griffiths M. Microstructural evolution of CANDU spacer material Inconel X-750 under in situ ion irradiation. J Nucl Mater 2013;443:49–58. https://doi.org/10.1016/j.jnucmat.2013.06.034.
[21] Judge CD, Bhakhri V, Jiao Z, Klassen RJ, Was G, Botton GA, et al. The effects of proton irradiation on the microstructural and mechanical property evolution of inconel X-750 with high concentrations of helium. J Nucl Mater 2017;492:213–26. https://doi.org/10.1016/j.jnucmat.2017.04.045.
[22] Cheng H, Kang L, Pang J, Xue B, Du D, Chang B. Effect of the welding position on weld quality when laser welding Inconel 617 Ni-based superalloy. Opt Laser Technol 2021;139:. https://doi.org/10.1016/j.optlastec.2021.106962106962.
[23] Sun J, Ren W, Nie P, Huang J, Zhang K, Li Z. Study on the weldability, microstructure and mechanical properties of thick Inconel 617 plate using narrow gap laser welding method. Mater Des 2019;175:. https://doi.org/10.1016/j.matdes.2019.107823107823.
[24] Sharma SK, Biswas K, Nath AK, Manna I, Dutta MJ. Microstructural change during laser welding of Inconel 718. Optik 2020;218:. https://doi.org/10.1016/j.ijleo.2020.165029165029.
[25] Ojo OA, Richards NL, Chaturvedi MC. Microstructural study of weld fusion zone of TIG welded IN 738LC nickel-based superalloy. Scripta Comput Sci Appl Math Materialia 2004;51:683–8. https://doi.org/10.1016/j.scriptamat.2004.06.013.
[26] Yan S, Meng Z, Chen B, Tan C, Song X, Wang G. Experimental study on the grain evolution induced by thermal characteristics during oscillation laser welding of IN718. Mater Lett 2022;323:. https://doi.org/10.1016/j.matlet.2022.132581132581.
[27] Ahmed MMZ, I. A. Habba M, Jouini N, Alzahrani B, Seleman MME-S, El-Nikhaily A. Bobbin Tool Friction Stir Welding of Aluminum Using Different Tool Pin Geometries: Mathematical Models for the Heat Generation. Metals 2021;11:438. https://doi.org/10.3390/met11030438.
[28] Ahmed MMZ, Ataya S, El-Sayed Seleman MM, Mahdy AMA, Alsaleh NA, Ahmed E. Heat Input and Mechanical Properties Investigation of Friction Stir Welded AA5083/AA5754 and AA5083/AA7020. Metals 2021;11:68. https://doi.org/10.3390/met11010068.
[29] Shao J, Yu G, He X, Li S, Chen R, Zhao Y. Grain size evolution under different cooling rate in laser additive manufacturing of superalloy. Opt Laser Technol 2019;119:. https://doi.org/10.1016/j.optlastec.2019.105662105662.
[30] Palanivel R, Dinaharan I, Laubscher RF, Alarifi IM. Effect of Nd:YAG laser welding on microstructure and mechanical properties of Incoloy alloy 800. Opt Laser Technol 2021;140:. https://doi.org/10.1016/j.optlastec.2021.107039107039.
[31] Shamanian M, Valehi M, Kangazian J, Szpunar JA. EBSD characterization of the L-605 Co-based alloy welds processed by pulsed Nd:YAG laser welding. Opt Laser Technol 2020;128:. https://doi.org/10.1016/j.optlastec.2020.106256106256.
[32] Lippold JC. Welding Metallurgy and Weldability. John Wiley & Sons; 2014.
[33] Shinozaki K, Wen P, Yamamoto M, Kadoi K, Kohno Y, Komori T. Effect of Grain Size on Solidification Cracking Susceptibility of Type 347 Stainless Steel during Laser Welding. Q J Jpn Weld Soc 2011;29. https://doi.org/10.2207/qjjws.29.90s. 90s-40s.
[34] Pariyar A, Perugu CS, Toth LS, Kailas SV. Microstructure and mechanical behavior of polymer-derived in-situ ceramic reinforced lightweight aluminum matrix composite. J Alloy Compd 2021;880:. https://doi.org/10.1016/j.jallcom.2021.160430160430.
[35] Pariyar A, Toth LS, Kailas SV, Peltier L. Imparting high-temperature grain stability to an Al-Mg alloy. Scripta Comput Sci Appl Math Materialia 2021;190:141–6. https://doi.org/10.1016/j.scriptamat.2020.08.035.